Research Square

Preprints are preliminary reports that have not undergone peer review.
They should not be considered conclusive, used to inform clinical practice,
or referenced by the media as validated information.

Automated cross-modal framework enables whole-brain mesoscale connectivity mapping in macaques

Pengcheng Li

pengchengli@mail.hust.edu.cn

Huazhong University of Science and Technology https://orcid.org/0000-0002-5695-9304

Zhuo Junjie

School of Biomedical Engineering, Hainan University

Zhanbo Zhang

Hainan University https://orcid.org/0009-0007-6746-8918

Chi Xiao

Hainan University

Mingli Wang

Institute of Neuroscience, Center for Excellence in Brain Science and Intelligence Technology, Chinese Academy of Sciences

Shukang Bi

Hainan University

Liang Shi

Hainan University https://orcid.org/0000-0002-4268-4784

Qingming Luo

Hainan University https://orcid.org/0000-0002-6725-9311

Hui Gong

HUST-Suzhou Institute for Brainsmatics, JITRI, Suzhou 215123, China https://orcid.org/0000-0001-5519-6248

Zhiming Shen

Center for Excellence in Brain Science and Intelligence Technology, Institute of Neuroscience https://orcid.org/0000-0003-4560-7650

Xiaoquan Yang

Hainan University

Technical Report

Keywords:

Posted Date: November 17th, 2026

DOI: https://doi.org/10.21203/rs.3.rs-10958613/v1

License: This work is licensed under a Creative Commons Attribution 4.0 International License.
Read Full License

Additional Declarations: There is **NO** Competing Interest.

Automated cross-modal framework enables whole-brain mesoscale connectivity mapping in macaques

Junjie Zhuo[1,6], Zhanbo Zhang[1,6], Chi Xiao[1], Mingli Wang[3,5], Shukang Bi[1], Liang Shi[1], Qingming Luo[1], Hui Gong[2], Zhiming Shen[3,4*], Xiaoquan Yang[1,2*], and Pengcheng Li[1,2*]

1. State Key Laboratory of Digital Medical Engineering, Key Laboratory of Biomedical Engineering of Hainan Province, School of Biomedical Engineering, Hainan University, Sanya. 572025;

2. HUST-Suzhou Institute for Brainsmatics Imaging, Chinese Academy of Medical Science, HUST-Suzhou Institute for Brainsmatics, JITRI, Suzhou, 215100;

3. Institute of Neuroscience, Center for Excellence in Brain Science and Intelligence Technology, Chinese Academy of Sciences, Shanghai 200031;

4. Shanghai Center for Brain Science and Brain-Inspired Technology, Shanghai 201602;

5. Lingang Laboratory, Shanghai 200031;

6. These authors contributed equally

** Correspondence: zmshen@ion.ac.cn, xyang@hainanu.edu.cn, and pengchengli@hainanu.edu.cn*

Abstract

Advances in whole-brain ex vivo imaging enable large-scale, cellular-resolution mapping of macaque brain architecture and connectivity. However, the seamless integration of multimodal datasets at scale remains challenging due to substantial tissue deformation, cross-modal contrast discrepancies, and individual morphological variability. Here, we present Macaca-Star, a high-throughput, fully automated framework for cross-modal whole-brain mapping in macaques. Macaca-Star synergizes modality-specific preprocessing, deep learning–based cross-modal translation, and optional subject-specific in vivo MRI guidance to achieve robust spatial and modal alignment. This end-to-end system reconciles these disparities, eliminates manual intervention and reduces the processing time from weeks to hours while maintaining high anatomical fidelity. It effectively maps both 3D volumetric and 2D section-based optical data into a unified anatomical space, enabling precise spatial integration of cytoarchitectural features, axonal projections, and neuronal somata. To demonstrate its discovery potential, we applied Macaca-Star to integrate fMOST-derived anterograde tracing with section-based retrograde tracing data. This integration resolved subregional connectivity patterns within the temporoparietal and insular areas that were previously difficult to unify across disparate imaging scales. Overall, Macaca-Star offers a versatile platform for multimodal data fusion, advancing comprehensive connectivity and atlas-based analysis in the primate brain.

Introduction

A fundamental goal of neuroscience is mapping the intricate architecture of the brain to understand cognition and disease(*1, 2*). Modern neurotechnologies generate massive datasets spanning multiple scales(*3*). These diverse data streams capture everything from cellular cytoarchitecture(*4, 5*) and spatial transcriptomics(*6, 7*) to long-range whole-brain connectivity(*8*). However, extracting biological meaning requires integrating these isolated, heterogeneous datasets into a unified anatomical framework(*9*). In rodent models, standardized reference atlases like the Allen Mouse Brain Common Coordinate Framework (CCFv3) successfully serve as this unifying hub(*10*). Automated computational frameworks routinely map diverse mouse brain data into this standard space(*11-13*). Conversely, achieving similar automated, cross-scale data integration for the non-human primate brain remains a monumental technical barrier(*14, 15*).

The macaque brain is a critical model for human neurobiology, yet integrating its multimodal data presents three specific challenges. First, the physical scale of tissue deformation is severe. The macaque brain is roughly 200 times larger than a mouse brain(*16*). Consequently, generating high-resolution ex vivo data requires extensive tissue processing, which causes massive non-uniform shrinkage and nonlinear warping(*17-19*). Second, a severe cross-modal domain gap exists. Prevailing macaque brain templates are predominantly MRI-based(*20, 21*). Conversely, the high-resolution optical imaging technologies necessary for cellular mapping lack MRI-like contrast. Third, inter-individual anatomical variability is highly pronounced. Cortical folding patterns and subcortical boundaries vary significantly across macaque subjects(*16, 22*). Attempting to map distorted ex vivo optical images directly to a standard space ignores these unique individual morphologies. Collectively, these compounding factors severely hinder the seamless integration of primate datasets.

Researchers have developed various strategies to address these issues. A standard approach uses block-face photography as an intermediate structural reference. This preserves 3D topological continuity during serial section reconstruction(*23*). To bridge the contrast gap, prior works employed modality-independent metrics like MIND(*24*) or image synthesis techniques(*25-27*). Recently, AI-assisted workflows such as BrainBuilder(*14*), Path2MR(*28*), and NextBrain(*29*) advanced MRI-like contrast synthesis for histology. Despite these

advancements, a robust framework tailored for ultra-large optical volumes remains lacking. Furthermore, while block-face imaging maintains section order, the captured brain has already undergone severe ex vivo deformations from skull removal and tissue fixation(*17, 23*). Therefore, intense texture disparities and unpredictable geometric distortions remain major hurdles for whole-brain mapping.

To overcome these intertwined hurdles, we developed Macaca-Star, a modular, deep learning–assisted framework designed for multimodal whole-brain mapping in macaques. It processes 3D fluorescence micro-optical sectioning tomography (fMOST) volumes(*30*) or serial 2D sections with paired block-face images(*31*). Extending standard block-face workflows, Macaca-Star integrates the mapping of 2D fluorescence sections and 3D optical datasets into standard atlas spaces through two core innovations. First, a deep learning module named CycWave-Mamba synthesizes accurate T1-weighted (T1w) contrasts directly from optical images. This converts a difficult cross-modal registration into a tractable intra-modal task. Second, when available, the framework utilizes a subject-specific in vivo MRI as a vital structural bridge. Block-face images inevitably contain unquantifiable ex vivo distortions. The in vivo MRI provides the ground truth for the undisturbed biological anatomy. Aligning synthesized volumes to this in vivo MRI absorbs tissue artifacts before final mapping to the NMT space. If in vivo T1w MRI are unavailable, the framework can register the synthesized volumes directly to the standard template. Crucially, the entire Macaca-Star framework operates fully automatically. It completes the precise spatial mapping of multi-terabyte 3D volumes or dense 2D sections in just one to three hours. By successfully integrating these massive datasets with exceptional speed, we demonstrate that Macaca-Star is a robust and highly scalable tool for constructing multimodal macaque connectomes. We have uploaded the relevant code on website (http://atlas.brainsmatics.org/a/zhuo2504).

Result

Overview of the Macaca-Star framework

We developed Macaca-Star, a modular framework designed to integrate multimodal whole-brain data and perform atlas-based analysis within a common macaque anatomical space (Fig. 1). The framework seamlessly combines diverse macaque brain datasets. These include high-resolution 3D optical volumes from fMOST, serial 2D fluorescence sections, block-face

images, and MRI data. By utilizing 2D and 3D cross-modal translation alongside reference-guided alignment, Macaca-Star enables the accurate mapping of PI-derived cytoarchitecture, GFP-labeled axonal projections, and retrogradely labeled neuronal somata into a standardized template space. To demonstrate its utility, we applied the framework to fMOST anterograde tracing and thick-section retrograde tracing datasets (Fig. 1).

The overall experimental procedure begins with subject-specific in vivo MRI acquisition for injection targeting, followed by viral injection, sample preparation, and ex vivo optical imaging (Fig. 1A). The acquired imaging data then undergo preprocessing tailored to specific imaging streams (Fig. S1). For section-based data, we processed 251 2D fluorescence sections, each measuring 62,208 × 82,134 pixels. These sections were paired with corresponding block-face photographs, followed by 3D reconstruction and soma localization. For whole-brain fMOST imaging, a representative dataset contained 19,998 serial sections with a matrix size of 125,123 × 81,953 pixels, totaling 183 TB for the PI structural channel and 33.3 TB for the GFP signal channel. To process these ultra-large volumes, the framework corrects image intensity on the PI structural channel to enable 3D reconstruction. Concurrently, it processes the GFP signal channel for neuron tracing.

To mitigate contrast and texture discrepancies across imaging modalities, Macaca-Star incorporates CycWave-Mamba, a cross-modal style transfer model. (Fig. 1B). For 3D optical datasets, this model translates reconstructed fMOST PI volumes and block-face volumes into synthetic T1w images. These synthetic images share a standardized contrast designed to match the NIMH Macaque Template (NMT). For section-based 2D data, the model converts fluorescence images into block-face-like representations. This conversion facilitates accurate registration between sections and block-face images to ensure reliable 3D reconstruction.

Macaca-Star leverages these synthetic T1-like images for flexible spatial registration into the standard NMT space (Fig. 1C). The framework supports two distinct registration pathways: direct registration of synthetic images to the NMT, or registration guided by subject-specific in vivo T1w MRI. This guided approach helps mitigate postmortem tissue deformation and individual anatomical variability. During this overall workflow, block-face volumes serve as physical intermediate references to properly align the 2D fluorescence sections. Finally, the framework applies the resulting non-linear deformation fields to map specific anatomical

features, including axonal projections and soma distributions, into the NMT space for integration and atlas-based analysis. Detailed workflows of the Macaca-Star are depicted in Fig. S2. This provides a unified platform for atlas-based quantification and statistical co-analysis.

Cross-modal style transfer via CycWave-Mamba

Reducing feature differences between imaging modalities is crucial for accurate cross-modal registration, particularly when aligning optical images like fMOST PI and block-face data to T1w target templates such as the NMT. Although preprocessing mitigates image artifacts and intensity inhomogeneities, pronounced brightness and texture discrepancies persist. To bridge these domain gaps, we developed CycWave-Mamba, an unsupervised cycle-consistent adversarial framework tailored for 3D volumetric cross-modal translation (Fig. 2A), alongside a 2D slice-wise version. Its architecture features dual generators that combine Discrete Wavelet Transform (DWT) feature separation with a hybrid ResNet-Mamba bottleneck. The framework also incorporates two spatial discriminators and a specialized texture discriminator for T1w image synthesis. While the 2D version efficiently handles slice-level data, the 3D formulation leverages volumetric spatial context to ensure structural continuity and preserve tissue topology. We trained dedicated CycWave-Mamba models for both fMOST PI and block-face modalities to ensure robust template alignment.

We validated the accuracy of CycWave-Mamba using quantitative correlation analyses. We compared both preprocessed optical volumes and synthetic T1w volumes against the reference NMT template (Fig. 2, E and F). For both fMOST PI and block-face datasets, our translation method substantially improved structural similarity to the NMT template. Specifically, for fMOST PI images, CycWave-Mamba markedly increased the Pearson correlation coefficient (r) with the NMT template from -0.55 to 0.94. The coefficient of determination (R^2) also improved from 0.30 to 0.88. For block-face images, the r value increased from 0.51 to 0.92, and the R^2 value rose from 0.26 to 0.85.

To assess inter-subject generalizability and statistical robustness, we next evaluated the model on an expanded macaque optical dataset comprising 10 fMOST PI and 5 blockface image volumes (Fig. S3A, B). Group-level analyses robustly confirmed this high synthesis fidelity. Compared to the native optical images, the synthetic T1w-like volumes achieved

significantly higher r and R^2 with the standard NMT template across both modalities (paired t-test, all $p < 0.001$; Fig. S3C, D). Specifically, for fMOST PI, image synthesis achieved high template consistency, yielding an r of 0.91 ± 0.03 and an R^2 of 0.82 ± 0.05, reversing the negative native PI contrast, which exhibited an r of -0.43 ± 0.09 and an R^2 of 0.19 ± 0.07. Similarly, for blockface imaging, synthetic volumes yielded an r of 0.92 ± 0.02 and an R^2 of 0.85 ± 0.03, compared to an r of 0.61 ± 0.07 and an R^2 of 0.38 ± 0.08 for the native data. Cross-subject evaluation further demonstrated consistent, high-quality translation across multiple anatomical planes for both volumetric 3D (Fig. S4) and slice-wise 2D (Fig. S5) implementations of CycWave-Mamba. Together, these results confirm that CycWave-Mamba faithfully preserves fine anatomical details and structural correspondence during cross-modal translation.

3D cross-modal registration accuracy in fMOST and block-face brains

To evaluate registration accuracy in native space, we mapped the standard NMT-defined CHARM cortical and SARM subcortical atlases onto individual fMOST-PI and block-face volumes at 50 μm isotropic resolution. Evaluating mapping precision in native space preserved fine anatomical details, thus providing a more rigorous basis for assessing registration quality. Qualitative inspection confirmed precise visual correspondence between mapped atlas boundaries and native anatomical structures across evaluated datasets, as demonstrated by representative fMOST-PI, blockface, and 3D-reconstructed fluorescence macaque brain volumes (Fig. 3A, Fig. S6).

To quantitatively assess registration performance relative to existing approaches, we compared Macaca-Star against deep learning-based SynthMorph, Modality-Independent Neighborhood Descriptor (MIND), classical ANTs with mutual information (ANTs-MI), and CycleGAN combined with ANTs using cross-correlation (CycleGAN+ANTs-CC). We evaluated these methods across 9 fMOST PI (Fig. 3B) and 5 block-face (Fig. 3D) macaque brains. We systematically evaluated registration accuracy across multiple anatomical levels. For the cortex, we used CHARM level 1 to assess the frontal, parietal, occipital, and temporal lobes. For the subcortex, we used SARM level 2 to assess the amygdala (Amy), lateral ventral pallidum (LVPal), medial pallidum (MPal), and thalamus (Thal). We also evaluated brainstem divisions (medulla, midbrain, and pons) alongside the cerebellum (Cb). Beyond volumetric overlap

measured by Dice scores (Fig. 3B, D), boundary accuracy was further validated via Surface Dice and Mean Surface Distance (MSD) (Fig. S7).

Quantitative evaluations demonstrated that our framework achieved well registration accuracy compared with alternative registration methods. On fMOST-PI volumes, Macaca-Star achieved an average median Dice score of 0.923, with region-wise median Dice scores ranging from 0.86 to 0.98 (Fig. 3B). This significantly outperformed compared methods, which only achieved scores ranging from 0.721 to 0.843 (Fig. 3B). Boundary accuracy metrics further confirmed this superior performance (Fig. S7A, B). Our method achieved Surface Dice scores ranging from 0.817 to 0.996, with a mean of 0.929. The MSD ranged from 0.035 to 0.309 mm, with an average median of 0.112 mm. Additionally, our framework demonstrated superior whole-brain registration performance for block-face brain volumes in both volumetric overlap (Fig. 3D) and boundary precision (Fig. S7C, D).

We further extended our quantitative evaluations to finer anatomical subdivisions at level 4 for both CHARM and SARM atlases. Specifically, we calculated Dice scores across representative cortical and subcortical regions, including the primary motor cortex (M1), premotor cortex (PM), visual areas (V1, V2, and V3), entorhinal cortex (ERh), and parahippocampal cortex (paraHipp). Subcortical targets included the claustrum (Cl), hippocampal formation (HF), intralaminar thalamus (ILTHal), pallidum (Pd), and the stria terminalis and amygdala subregion (stAmy). For fMOST PI volumes, our method achieved region-wise median Dice score ranging from 0.82 to 0.95, with average median Dice score reached 0.885 (Fig. S7E). This represents an approximate 19% improvement over other methods, which ranged from 0.585 to 0.741. Similar performance gains were observed on 3D block-face brains (Fig. S7F).

Finally, we evaluated the specific contribution of subject-specific in vivo MRI guidance. We compared our full framework against an MRI-free strategy. This evaluation utilized average Dice scores from the fine level 4 subdivisions across all subjects. For fMOST PI volumes, the MRI-guided strategy achieved an average median Dice score of 0.893 (Fig. 3C), compared with 0.827 for the MRI-free strategy. For block-face brains, the MRI-guided score reached 0.939 compared to 0.826 for the MRI-free approach (Fig. 3E). Both comparisons demonstrated statistically significant improvements (paired t-test, $p < 0.01$). This confirms the

necessity of MRI guidance for resolving severe ex vivo deformations.

2D Fluorescence slices Registration accuracy

Traditional 2D histological slices often suffer from severe irregular distortions. To overcome this, our framework utilizes block-face images as intermediate physical references. Specifically, we aligned each highly distorted 2D fluorescence section to its corresponding 2D block-face slice, thereby effectively correcting local deformations and achieving high-precision 3D fluorescence volume reconstruction (Fig. 3a, right panel).

To quantitatively evaluate this 2D registration accuracy, we performed landmark-based analysis. Expert anatomists manually annotated paired landmarks across corresponding anatomical structures, linking the original block-face sections and registered fluorescence slices, as presented within the 3D macaque brain topology (Fig. 3F). A total of 708 paired landmarks were broadly distributed across four cortical lobes, including 194 in the occipital, 168 in the frontal, 105 in the temporal, and 87 in the parietal lobe, alongside 129 in the subcortex and 25 in the brainstem (Fig. 3G). Their representative slice locations are illustrated in Fig. S8.

We calculated the Euclidean distance between these paired landmarks to determine the local registration error. The magnitude distribution of 2D landmark registration errors across fluorescence sections demonstrated high spatial fidelity, with a mean error of 0.097 mm, a standard deviation of 0.316 mm, and a standard error of 0.012 mm (Fig. 3H). These quantitative results confirm that Macaca-Star effectively recovers non-linear tissue distortions in 2D slices and accurately maps them into the unified 3D atlas space.

Robustness of MRI-guided registration for partial brain volumes

Ex vivo preparation may result in tissue loss, while some studies require only contiguous partial-brain sections rather than whole-brain data. We therefore evaluated the robustness of Macaca-Star for partial brain volume registration. Partial fMOST and block-face volumes were generated by progressively truncating the anterior and posterior portions of the whole-brain datasets, with truncation ratios ranging from 20% to 80% (Fig. 4A, C). Quantitative evaluation using cortical and subcortical masks, merged respectively from CHARM and SARM, revealed that the MRI-guided strategy maintained consistently stable performance across truncation ratios, whereas the accuracy of the MRI-free strategy degraded severely (Fig. 4B,

D).

Overall, the average median Dice score for the MRI-free strategy dropped from 0.91 at 20% truncation to 0.73 at 80% truncation, whereas the MRI-guided strategy maintained stable high scores between 0.92 and 0.93 across all evaluated truncation ratios. Specifically, for the cortical mask, the average median Dice score for the MRI-free strategy dropped sharply from 0.88 at 20% truncation to 0.68 at 80% truncation. In contrast, the MRI-guided strategy remained resilient, achieving stable average median Dice scores between 0.89 and 0.90. Similarly, for the subcortical mask, the MRI-guided strategy consistently sustained high scores ranging from 0.94 to 0.95, whereas the MRI-free strategy score declined from 0.94 to 0.79.

Qualitative evaluation further corroborated these quantitative findings; registered partial brain volumes at different truncation ratios were transparently overlaid onto the NMT reference template (Fig. 4E), demonstrating stable anatomical correspondence and preservation of morphological boundaries within the retained volume, even at the highest truncation ratio.

Multimodal atlas integration of cortical circuits

To demonstrate the capacity of our framework in integrating multimodal neuroanatomical information, we mapped fMOST 3D axonal projection pathways and 2D fluorescence sectional soma distributions into a unified standard stereotaxic space (Fig. 5). An integrated 3D visualization combined GFP-labeled projection pathways from four distinct injection sites. This comprehensive map revealed clear spatial segregation and target innervation patterns across anterior, superior, and lateral orthogonal views (Fig. 5A). Complementing this overall map, individual 3D reconstructions further delineated site-specific axonal trajectories, highlighting annotated injection locations and their respective target brain regions (Fig. 5B). Axonal projections originating from additional injection sites are provided in the Supplementary Information (Fig. S9). Furthermore, the cortical laminar organization at the primary motor cortex (M1) injection site was characterized in native space, delineating five distinct laminae with layers III and IV merged into a single layer (Fig. 5C).

Two Ri-centered injections were first examined to characterize their whole-brain projection patterns (Fig. 5B). Despite differences in the overall distribution of labeled fibers, consistent labeling was identified in the secondary somatosensory cortex (SII), granular insula (Ig), and

temporoparietal area (Tpt) in both injections. Additional labeled territories included the caudomedial auditory belt (CM) following the left-hemisphere injection, and superior parietal area (PE), posterior medial parietal area (PGm), and medial superior temporal area (MST) following the right-hemisphere injection.

The Ig was consistently identified in both injections. Additional labeling was observed in superior parietal area PE (PE), posterior medial parietal area PGm (PGm), and posterior cingulate area 23b (23b) in one injection, whereas the other showed labeling in the medial pulvinar (MPul). Additional labeled regions were observed across individual injections and are presented in the corresponding figures.

A right M1-centered injection revealed labeled fibers in ventral premotor areas F4 and F5, the posteroventral part of the ventrolateral thalamic nucleus (VLPV), the putamen (Pu), and primary somatosensory areas 1–2 (Fig. 5B). Together, these observations demonstrate that the framework captures distributed projection patterns spanning cortical and subcortical territories across different injection sites.

To further quantify the relative contribution of different source regions, the fraction of extrinsic labeled neurons (FLNe) was calculated from the mapped retrogradely labeled somata following injections into the merged dysgranular and agranular insula (Id/Ia) and Ig (Fig. 5F, G). These two injections exhibited heterogeneous connectivity profiles. The FLNe values spanned approximately four orders of magnitude. Both ipsilateral and contralateral source regions provided substantial contributions.

For the Id/Ia injection, strong inputs (FLNe > 0.01) accounted for 78.0% of the total extrinsic labeled neurons. The largest single contribution arose from the ipsilateral Ig (FLNe = 0.199). Other major ipsilateral inputs included the parainsular area (Pi, 0.070), claustrum (Cl, 0.057), precentral opercular area (PrCO, 0.052), intermediate agranular insula (Iai, 0.051), and SII (0.047) (Fig. 5F). Contralateral inputs accounted for 11.5% of the total FLNe. The strongest contralateral inputs came from the Id/Ia (0.043) and Ig (0.015). Additional contralateral contributions arose from Pi, Cl, parietal opercular area 7op, posterior cingulate area 24c, F5, temporoparieto-occipital area (TPO), and SII. For the Id injection, strong inputs (FLNe > 0.01) accounted for 78.0% of the total extrinsic labeled neurons. The largest single contribution arose from the ipsilateral Ig (FLNe = 0.199). Other major ipsilateral inputs included the

parainsular area (Pi, 0.070), claustrum (Cl, 0.057), precentral opercular area (PrCO, 0.052), intermediate agranular insula (Iai, 0.051), and SII (0.047) (Fig. 5F). Contralateral inputs accounted for 11.5% of the total FLNe. The strongest contralateral inputs came from the Id (0.043) and Ig (0.015). Additional contralateral contributions arose from Pi, Cl, parietal opercular area 7op, posterior cingulate area 24c, F5, temporoparieto-occipital area (TPO), and SII.

The Ig injection showed a similarly concentrated input profile. Strong inputs accounted for 70.4% of the total FLNe. The ipsilateral Id provided the largest contribution (FLNe = 0.204). This was followed by Cl (0.093), rostromedial auditory belt (RM, 0.072), Pi (0.064), and 7op (0.057) (Fig. 5G). Contralateral sources contributed 14.9% of the total FLNe for the Ig injection. The largest contralateral contributions arose from Id (0.031), Ig (0.030), 7op (0.0095), RM (0.0093), Cl (0.0092), and CM (0.0080). Various auditory, temporal, parietal, and cingulate regions provided additional minor inputs.

Finally, retrogradely labeled neurons were identified bilaterally in the Tpt following both injections. This demonstrates definitive Tpt inputs to both Id and Ig. However, the Tpt contribution to Ig was substantially greater than to Id. Overall, a relatively small subset of high-weight inputs dominated the FLNe profiles. Simultaneously, these profiles revealed highly distributed interhemispheric connectivity. Notably, a strong reciprocal anatomical relationship emerged. Ig provided the strongest extrinsic input to Id, and conversely, Id provided the strongest extrinsic input to Ig (Fig. 5, H and I). For additional injection sites, retrograde soma locations are detailed in Fig. S10.

Discussion

We established Macaca-Star as an automated, highly robust framework for integrating multimodal macaque neuroanatomical data. The framework uniquely combines deep learning-based cross-modal translation with flexible, optional subject-specific in vivo MRI guidance. Previous rodent studies relied on image style transfer(*11*), whereas non-human primate studies(*19, 23*) depended solely on MRI guidance. Our quantitative results demonstrate that neither approach alone suffices for the highly convoluted macaque brain. CycWave-Mamba successfully resolves the cross-modal domain gap by synthesizing T1w representations from optical images. When available, the subject-specific in vivo MRI provides

the physical ground truth to resolve complex ex vivo sample deformations. Combining these complementary approaches provides a robust solution for accurate data integration across both cortical and subcortical regions.

Histological and biomedical studies frequently encounter incomplete datasets(*27, 29*), due to tissue loss during sample preparation or experimental designs that target specific anatomical regions(*32*). As a result, only a limited series of contiguous sections may be available rather than complete whole-brain volumes(*33*). Such partial datasets can substantially increase the difficulty of registration by reducing the available anatomical context. Our partial-volume experiments demonstrate that Macaca-Star remains robust under these conditions. By incorporating the subject-specific in vivo MRI as a global structural anchor, the framework maintained highly accurate anatomical boundaries even at an 80% truncation ratio (Fig 4.). While our current empirical validation focuses on primate neuroanatomy, the underlying conceptual framework addresses challenges that are broadly encountered in 3D histological reconstruction and registration(*17*). At its core, the framework couples AI-driven cross-modal image synthesis with macroscopic anatomical constraints to facilitate spatial correspondence across disparate imaging modalities. Owing to its modular design, this architecture can be readily extended to align incomplete histological samples from other large species(*5, 29, 34*) or diverse organ systems(*17*).

Macaca-Star unites CycWave-Mamba cross-modal synthesis, macroscopic MRI anchoring, and ANTs-based non-linear registration(*35*) into a fully automated framework. This specific architecture successfully bridges the massive modality and geometry gaps inherent to macaque brain processing(*17*). Crucially, the trained CycWave-Mamba model exhibits robust cross-modal generalizability across diverse optical imaging protocols without requiring case-specific retraining. Macaca-Star also reduces the computational and manual burden associated with large-scale optical imaging data. Conventional processing of multi-terabyte datasets can require substantial user intervention and lengthy computation(*36*). In contrast, Macaca-Star provides a fully automated workflow for spatial normalization of both fMOST volumes and fluorescence sections into a common reference space, with typical processing times of approximately 2–4 hours. Another critical advantage of this framework is its bidirectional mapping capability. The framework accurately registers individual optical volumes into the common reference space while projecting standard atlas parcellations back

into the native individual space. This feature preserves in situ spatial context, enabling applications like single-neuron reconstruction(*15, 30*) and spatial transcriptomics analysis(*6, 37*).

Beyond methodological validation, Macaca-Star serves as a powerful engine for biological discovery. We successfully integrated fMOST 3D axonal projection pathways and 2D fluorescence soma distributions into a unified coordinate system. Our bidirectional tracing results largely aligned with established neuroanatomical literature. Furthermore, incorporating fMOST data unlocks a crucial spatial capability. Macaca-Star not only verifies inter-regional connectivity, but also resolves continuous 3D axonal trajectories from source to target regions. By mapping retrogradely labeled somata, we further quantified FLNe-based connectivity profiles(*38*) for Ia/Id and Ig. These profiles revealed substantial interhemispheric inputs and strong reciprocal connectivity between Ig and Ia/Id. Notably, our bidirectional tracing approach independently confirmed projections from Tpt to Ia/Id. Although previous tracer studies have documented broader connectivity between temporal association regions and Ia/Id, a direct Tpt-to-Ia/Id projection has not been specifically characterized (*39-42*). At a macroscale, diffusion tensor imaging has also suggested structural connectivity within this broader temporo-insular network(*43*), but cannot establish pathway direction or provide cellular-level anatomical detail. By combining anterograde and retrograde tracing, our results provide convergent anatomical support for a Tpt-to-Ia/Id projection.

We acknowledge certain data requirements and limitations in the current framework. Optimal registration benefits from densely sampled optical volumes and subject-specific in vivo MRI. Although subject-specific MRI may not be available for all datasets, such imaging is increasingly incorporated into large-animal studies for injection planning and probe localization (*30, 44, 45*). When in vivo MRI is unavailable, Macaca-Star provides a robust alternative by registering synthesized volumes directly to the NMT template. A further limitation concerns the delineation of small subcortical nuclei(*46-48*). The MRI-derived NMT template does not always provide sufficient anatomical detail to resolve boundaries that remain distinguishable in high-resolution optical images. Future development of ultra-high-resolution optical templates for the macaque brain could help resolve this intrinsic bottleneck. Ultimately, Macaca-Star provides an open-source and highly scalable foundation for constructing comprehensive multimodal primate connectomes.

MATERIALS AND METHODS

Animal care and use

All macaque experiments for the fMOST dataset were approved by the Institutional Animal Ethics Committee of Huazhong University of Science and Technology (Approval No. S166). Experiments conducted at the Institute of Neuroscience were approved by the Ethics Committee of the Institute of Neuroscience, Chinese Academy of Sciences (Approval Nos. ION-2019009 and CEBSIT-2020022).

Data preparation

The NMT v2.0 standard template(*20, 49*), along with the CHARM(*50*) and SARM(*47*) atlases, was obtained from AFNI. The NMT is an in vivo macaque brain MRI template at 250-μm isotropic resolution, providing tissue segmentations for gray matter, white matter, and cerebrospinal fluid. Both the cortical CHARM atlas and the subcortical SARM atlas feature six hierarchical scales (Levels 1–6), delineating 134 and 206 subregions at Level 6, respectively. In this study, Level 6 was adopted for all neuroanatomical analyses, including soma mapping and axonal projection profiling.

The fMOST dataset comprises whole-brain serial-sectioning data from 9 macaques across two simultaneously acquired channels: a PI structural channel and a GFP signal channel. The PI channel provides cytoarchitectonic contrast and serves as an anatomical reference. Concurrently, the GFP channel captures AAV-labeled anterograde projection pathways for axon tracing, relying on the simultaneously acquired PI channel for spatial alignment to templates or MRI. Across two macaques, the analyzed injection sites included bilateral Ri, M1, two ipsilateral sites in Tpt, areas 1–2, and bilateral area 44. In addition, in vivo T1w MRI data were acquired for six macaques prior to fMOST imaging at an isotropic resolution of 0.5 mm (TR = 10.56 ms, TE = 3.6 ms, flip angle = 10°, 3 averages). Comprehensive descriptions of sample preparation and fMOST imaging protocols have been reported previously.

In this study, retrograde tracing experiments were performed in 5 adult cynomolgus macaques, with targeted injection sites including Ia/Id, Ig, and two ipsilateral sites in V1. Prior to tracer injections, in vivo T1w MRI data were acquired for each macaque at an isotropic resolution of 0.5 mm (TR = 2200 ms, TE = 2.8 ms, flip angle = 9°, 4 averages). To achieve accurate 3D reconstruction, block-face photographs were captured prior to sectioning and

subsequently paired with 2D fluorescence sections for soma localization of retrogradely labeled neurons. Surgical, tracer injection, and histological protocols followed procedures detailed in previous studies.

fMOST preprocessing

Striping artifact removal. To robustly and rapidly remove striping artifacts, we implemented a focal-plane fitting method at a downsampled resolution of 50 × 50 × 50 $m\mu^3$ (Fig. S11A). Specifically, artifact correction was performed as follows: (1) Resampling: The original 2D section stack was reconstructed into a 3D volume and downsampled to an isotropic resolution of 50 mμ. (2) Projection: The reconstructed 3D volume was projected onto the section plane and averaged to obtain a mean projection image. (3) Profile extraction: An axis perpendicular to the stripe artifacts was selected, along which the signal intensity was projected and averaged to derive a 1D intensity profile, C(x). (4) Peak detection: Local maxima along C(x) were identified by defining thresholds for minimum peak height, peak width, and inter-peak distance. (5) Baseline fitting: The identified peaks were fitted using a Bessel function to construct a smoothed baseline curve, $C_b(x)$. (6) Gain normalization: A correction function was computed as ratio(x) = $C_b(x)$ / C(x). (7) Image restoration: The correction function was applied across the image to restore uniform intensity. Steps 3–6 were then repeated to remove artifacts on the opposite side of the image. The effectiveness of this correction was quantitatively verified by a marked decrease in the standard deviation of first-order differences (Fig. S11B).

Preprocessing for 2D fluorescent sections

Segmentation of the Consecutive 2D block-face images. Prior to tissue sectioning, block-face photographs were captured for each slice to preserve 3D morphological integrity. To isolate brain tissue from non-brain regions (e.g., embedding media), we segmented the consecutive block-face images using the Segment Anything 2 (SAM2) (*51*) model (Fig. S12A). Taking advantage of the structural continuity across adjacent serial sections, we treated the block-face sequence as continuous video frames. SAM2's memory attention and memory bank mechanisms allowed spatial prompts and mask predictions from preceding sections to condition subsequent frames, enabling robust and efficient brain tissue segmentation across the entire dataset.

SAM2 was initialized with pre-trained weights and subsequently fine-tuned on macaque block-face datasets. To leverage the spatial continuity of serial sections, we adopted an alternating training strategy that sampled both individual static frames and contiguous section sequences formatted as pseudo-videos. For video-mode training, contiguous slice sequences were sampled starting from the central section with the maximum cross-sectional area and progressing bidirectionally toward the anterior and posterior poles. Annotation ground truth was established via a human-in-the-loop framework: images initially underwent prompt-free automatic segmentation, after which sub-optimal masks were manually inspected and refined by providing interactive prompts (Fig. S12B).

3D block-face reconstruction. During block-face imaging, mechanical movements of the imaging platform and tissue, combined with coronal bisection of the macaque brain into anterior and posterior blocks, introduced spatial offsets between consecutive slices, impeding direct 3D volume reconstruction (Fig. S12E). To rectify these disruptions, we first computed the mean squared error (MSE) between adjacent slices to pinpoint the exact slice indices where abrupt offsets occurred (Fig. S12D):

$$MSE = \frac{1}{N}\sum_{i=1}^{N}(x_i - y_i)^2$$

where N denotes the total number of pixels per slice, and x_i and y_i represent the pixel intensity values at corresponding spatial coordinates in adjacent slices.

Once offset boundaries were identified, we centered the block-face slices and aligned the first displaced slice with its preceding neighbor via translational shifting. The remaining slices within the same offset block were then corrected by applying the identical translation vector (Fig. S12C). To compensate for secondary affine deformations caused by relative displacement between the tissue block and camera, an affine transformation matrix was estimated between the first offset slice and its adjacent reference slice. This matrix was subsequently applied to all subsequent slices in that block, yielding a fully aligned 3D block-face reconstruction (Fig. S12F).

3D reconstruction of serial fluorescent sections. We developed a 3D reconstruction framework to align serial fluorescent tissue sections using the reconstructed 3D block-face volume as a pre-sectioning spatial reference (Fig. S13A). First, to bridge the cross-modal domain gap, we employed our proposed 2D CycWave-Mamba model to translate fluorescent

section images into the block-face modality, generating synthetic block-face images. Global alignment was then achieved by affine registration between the synthetic images and their corresponding physical block-face counterparts. However, physical sectioning frequently caused tissue structures, such as the bilateral hemispheres and temporal lobes, to detach and shift substantially from their native anatomical positions. This introduced large spatial displacements that direct non-linear registration could not resolve. To address this limitation, we implemented a watershed-based segmentation method to partition both fluorescent and block-face slices into independent anatomical sub-regions. These detached sub-regions were then individually realigned guided by the synthetic images, restoring displaced tissue structures to their correct spatial positions (Fig. S13B). The resulting composite transformations, comprising cascaded affine matrices and non-linear deformation fields, enabled bidirectional mapping between standard brain atlases, raw fluorescent slices, and reconstructed soma coordinates in standard space.

Cross-modal synthesis of macaque brain images

The overall architecture for cross-modal brain image synthesis is CycWave-Mamba (Fig. 2), a wavelet-guided bidirectional translation network designed to synthesize target T1w MRI volumes from optical brain datasets. Based on the bidirectional CycleGAN(*52*) framework, we introduced wavelet transforms and an axis-shared 3D state-space model (Mamba)(*53*) into the generator backbone (Fig. 2A). In this architecture, the low-frequency components govern macroscopic intensity translation. Meanwhile, the high-frequency directional subbands are modulated by the Wavelet Modal Mapper (Fig. 2B) to adapt anatomical boundaries and fine-scale textures toward the target modality.

Generator architecture. The generator adopts an encoder–bottleneck–decoder architecture with wavelet-based skip connections. (Fig. 2A). Given an input optical volume $X \in R^{C_{in} \times D \times H \times W}$, shallow representations are first extracted through a 7 × 7 × 7 convolution with replication padding, followed by Instance Normalization and SiLU activation. The feature representation then passes through two progressive wavelet-integrated encoder blocks. Within each block, the feature map is decomposed using a wavelet transform into one low-frequency component and directional high-frequency subbands. The low-frequency component is passed to the subsequent encoder pathway and processed through a 3 × 3 ×

3 convolution to expand channel capacity, scaling feature dimensions from 48 to 96, and finally to 192 channels at the bottleneck entrance. In contrast, the high-frequency subbands are processed by a dedicated wavelet-domain transformation module, the Wavelet Modal Mapper, and stored as skip features for subsequent multi-scale reconstruction.

The bottleneck employs a hybrid design with an axis-shared 3D Mamba module sandwiched between 3D ResNet blocks(*54*). This structure captures long-range 3D anatomical dependencies while avoiding the prohibitive computational complexity of standard self-attention. The Mamba module scans the 3D feature representation sequentially along depth (D), height (H), and width (W) axes using a shared Mamba module. The outputs from the three axes are dynamically combined using learnable axis-weight coefficients:

$$F_{fused} = \mathcal{P}_{1\times1\times1}\big(w_d \cdot M_D(F) + w_h \cdot M_H(F) + w_w \cdot M_W(F)\big) + F$$

where F denotes the input feature map entering the Mamba module, w_d, w_h, w_w denote learnable weighting scalars, $M_{(\cdot)}$ represents directional Mamba operations along each corresponding axis, and $\mathcal{P}_{1\times1\times1}$ denotes a point-wise linear projection.

In the decoder, the low-frequency features are progressively combined with the transformed high-frequency subbands through multi-level inverse wavelet reconstruction to recover full-resolution feature representations. A final 7 × 7 × 7 convolution followed by a Tanh activation is then applied to generate the synthesized target-modality brain volume.

Wavelet modal mapper. To mitigate cross-modal contrast discrepancies, the high-frequency subbands $H_l \in R^{C\times K\times D\times H\times W}$ $(K = 3)$ extracted via plane-wise 2D wavelet decomposition are transformed by the Wavelet Modal Mapper (Fig. 2B). The subbands are first reshaped to $C \cdot K$ channels and processed by a convolutional stream $\mathcal{F}(\cdot)$ comprising grouped mixing, depthwise, and pointwise convolutions. The resulting features are then dynamically modulated by a channel attention branch $\mathcal{G}(\cdot)$. The adapted skip representation $\widetilde{H_l}$ is formulated as:

$$\widetilde{H_l} = \alpha \odot H_l + s \odot \big(\mathcal{F}(H_l) \odot \mathcal{G}(H_l)\big)$$

where α denotes the learnable subband-wise scaling parameter initialized to accommodate contrast polarity reversals, s represents the residual scaling factor, $\mathcal{G}(\cdot)$ denotes the channel attention module, and $\odot$ represents element-wise multiplication with broadcasting.

Discriminator architecture. The discriminator framework employs a dual-domain supervision strategy. It comprises a bidirectional Spatial Discriminator (D_s) and a target-specific Wavelet Texture Discriminator (D_t) dedicated exclusively to the T1w MRI domain ($\mathcal{Y}$). While D_s evaluates local anatomical realism across both domains, D_t operates directly in the wavelet domain to enforce sharp tissue boundaries and compel the recovery of fine-scale anatomical structures in synthesized MRI volumes.

The Spatial Discriminator (Fig. 2D) is deployed symmetrically for both domains ($D_{s,X}$ and $D_{s,Y}$) using a 3D PatchGAN(*55*) architecture that evaluates realism over local volumetric receptive fields. It consists of progressive strided 3D convolutional layers, normalization layers, and LeakyReLU activations ($\alpha = 0.2$), hierarchically expanding feature channels while downsampling spatial resolution. To expand the effective receptive field while maintaining parameter efficiency, 3D Wavelet Convolution (WTConv3d)(*56*) blocks are incorporated into the intermediate layers. A final convolutional Patch Head projects the resulting feature volume into a single-channel 3D logit map, where each voxel represents the validity prediction of a local 3D patch.

The Wavelet Texture Discriminator (D_t, Fig. 2C) is dedicated exclusively to the target MRI domain ($\mathcal{Y}$) to provide frequency-domain adversarial supervision, preventing standard patch discriminators from oversmoothing subtle anatomical details. Given an input 3D volume (real y or synthesized $\hat{y} = G_{X \to Y}(x)$), a discrete wavelet transform decomposes it into a low-frequency component L and three directional high-frequency subbands. The high-frequency subbands and their absolute values $[H, |H|]$ are fed into a spectral-normalized convolutional branch to evaluate directional edges and intensity gradients. Concurrently, the low-frequency component L is passed through a lightweight convolutional stream to retain coarse structural context. To prioritize high-frequency boundary refinement, the low-frequency feature is down-weighted before fusion:

$$F_{tex} = F_{high} + \beta \cdot F_{low}$$

where F_{high} and F_{low} denote the high- and low-frequency feature representations, respectively, and β is a small weighting scalar. A final convolutional prediction head projects the fused feature F_{tex} into a single-channel 3D patch-level logit map.

Training objectives and loss functions. Accordingly, the overall loss function $\mathcal{L}_{total}$ for

cross-modal brain synthesis includes the dual-domain adversarial losses, the bidirectional cycle-consistency loss, and the structural similarity constraint, which can be formulated as:

$$\mathcal{L}_{total} = \mathcal{L}^{s}_{GAN}\left(G_{X\to Y}, D_{s,Y}, X, Y\right) + \mathcal{L}^{s}_{GAN}\left(G_{Y\to X}, D_{s,X}, Y, X\right) + \mathcal{L}^{t}_{GAN}(G_{X\to Y}, D_t, X, Y) + \lambda_{cyc}\mathcal{L}_{cyc}(G_{X\to Y}, G_{Y\to X}) + \lambda_{ssim}\mathcal{L}_{ssim}(G_{X\to Y}, G_{Y\to X})$$

We adopt the least-squares adversarial formulation (LSGAN)(*57*) to stabilize training dynamics. The spatial adversarial objective for the forward mapping $G_{X\to Y}$ is formulated as:

$$\mathcal{L}^{s}_{GAN}\left(G_{X\to Y}, D_{s,Y}, X, Y\right) = E_{y\sim p_{data}(y)}\left[\left(D_{s,Y}(y) - 1\right)^2\right] + E_{x\sim p_{data}(x)}\left[\left(D_{s,Y}\left(G_{X\to Y}(x)\right)\right)^2\right]$$

The reverse spatial adversarial loss $\mathcal{L}^{s}_{GAN}\left(G_{Y\to X}, D_{s,X}\right)$ and the target-specific Wavelet Texture adversarial loss $\mathcal{L}^{t}_{GAN}(G_{X\to Y}, D_t)$ are defined analogously.

To enforce geometric bijection and prevent anatomical distortions in unpaired translation, the bidirectional cycle-consistency loss combines voxel-wise L_1 intensity constraints with local structural similarity (SSIM) penalties:

$$\mathcal{L}_{cyc}(G_{X\to Y}, G_{Y\to X}) = E_{x\sim p_{data}(x)}\left[\left|G_{Y\to X}\left(G_{X\to Y}(x)\right) - x\right|_1 + \alpha\left(1 - \mathrm{SSIM}\left(G_{Y\to X}\left(G_{X\to Y}(x)\right), x\right)\right)\right] + E_{y\sim p_{data}(y)}\left[\left|G_{X\to Y}\left(G_{Y\to X}(y)\right) - y\right|_1 + \alpha\left(1 - \mathrm{SSIM}\left(G_{X\to Y}\left(G_{Y\to X}(y)\right), y\right)\right)\right]$$

where $\mathcal{L}^{s}_{GAN}$ and $\mathcal{L}^{t}_{GAN}$ indicate the spatial adversarial loss and the wavelet texture adversarial loss, respectively. $G_{X\to Y}$ and $G_{Y\to X}$ denote the forward and backward generators, while $D_{s,X}$, $D_{s,Y}$, and D_t denote the optical spatial discriminator, MRI spatial discriminator, and MRI wavelet texture discriminator, respectively. X and Y indicate the optical microscopy volume dataset and T1w MRI volume dataset, with $x \sim p_{data}(x)$ and $y \sim p_{data}(y)$ representing their underlying data distributions. $\mathrm{SSIM}(\cdot,\cdot)$ measures the structural similarity within local 3D volumetric sliding windows. The weighting hyperparameters were empirically set to $\lambda_{cyc} = 10.0$ and $\alpha = 5$.

In our implementation, we developed two model variants for cross-modal brain synthesis, including a 3D volumetric version and a 2D slice-wise version, where the 2D network architecture and loss formulation are similar to the 3D design by reducing volumetric operations to their 2D counterparts.

Specifically, the 3D model was trained on cropped patches of size 128 × 64 × 128 voxels, while the 2D model used coronal slices with an input size of 512 × 512 pixels, both with a

batch size of 2. In both model variants, the initial feature channels for generators and discriminators were set to 48. All networks were optimized using the Adam optimizer with an initial learning rate of 0.0002. The 3D model was trained with the learning rate maintained constant for the first 200 epochs and decayed linearly to zero over the subsequent 100 epochs, whereas the 2D model was trained for 150 constant epochs and 100 decay epochs.

T1w synthesis-assisted whole-brain registration

To achieve accurate cross-modal data integration, we established two distinct registration strategies leveraging synthetic T1w-like images, including subject-specific in vivo MRI-guided registration and direct synthetic T1w-based registration (Fig. S14).

Subject-specific in vivo MRI-guided registration. In this strategy, the subject-specific in vivo MRI serves as an intermediate anatomical reference to bridge the optical modalities and standard stereotaxic space through a two-stage registration. In the first stage, both the synthetic T1w-like images and the NMT template were independently registered to the skull-stripped subject-specific in vivo T1w MRI (MRI processing framework detailed in Fig. S15). In the second stage, the two resulting MRI-space volumes were deformably registered to each other.

Through this two-stage registration strategy, each pairwise registration yields a composite spatial transformation consisting of an affine mapping A and a symmetric diffeomorphic transformation $\phi \in \mathrm{Diff}_0$. The overall composite transformation Φ mapping coordinates from native optical space to the standard NMT template space is formulated as:

$$\Phi = \Phi_2^{-1} \circ \phi_3 \circ \Phi_1 = (\phi_2 \circ A_2)^{-1} \circ \phi_3 \circ (\phi_1 \circ A_1)$$

where $\Phi_1 = \phi_1 \circ A_1$ denotes the composite transformation from native optical space to intermediate in vivo MRI space, $\Phi_2 = \phi_2 \circ A_2$ denotes the composite transformation from NMT template space to intermediate in vivo MRI space, and ϕ_3 represents the non-linear diffeomorphic refinement between the two intermediate MRI-space volumes. The operator $\circ$ denotes function composition.

Consequently, the transformed volume I_{NMT} and mapped atlas labels L_{opt} are computed via standard backward warping:

$$I_{NMT} = I_{opt} \circ \Phi^{-1}, \quad L_{opt} = L_{NMT} \circ \Phi$$

Specifically, each registration was performed using a global affine transformation followed by non-linear deformable registration. First, global alignment was achieved by minimizing the global correlation (GC) metric:

$$GC(f,m) = -\frac{\langle f-\bar{f}, m-\bar{m}\rangle^2}{\|f-\bar{f}\|_2^2 \cdot \|m-\bar{m}\|_2^2}$$

where f and m denote the voxel intensity vectors of the target reference and moving volume, respectively, with $\bar{f}$ and $\bar{m}$ denoting their mean intensities. The notation $\langle\cdot,\cdot\rangle$ represents the vector inner product. The affine optimization was performed with a metric sampling parameter of 32, a random sampling rate of 0.2, and multi-resolution iterations of 2100 × 1200 × 1200 × 10 across pyramid levels.

Subsequently, Symmetric Normalization (SyN) was performed at an isotropic resolution of 250 × 250 × 250 mm^3 using the cross-correlation (CC) metric:

$$CC(f,m) = -\frac{\sum_x\left(\sum_{y\in\mathcal{N}(x)}(f(y)-\bar{f_x})(m(y)-\overline{m_x})\right)^2}{\sum_x\left(\sum_{y\in\mathcal{N}(x)}(f(y)-\bar{f_x})^2 \cdot \sum_{y\in\mathcal{N}(x)}(m(y)-\overline{m_x})^2\right)}$$

where $\mathcal{N}(x)$ denotes the local spatial neighborhood centered at voxel x, y indexes the voxels within this neighborhood $\mathcal{N}(x)$, while $\bar{f_x}$ and $\overline{m_x}$ represent the local mean voxel intensities of the reference volume f and the deformed moving volume m within $\mathcal{N}(x)$, respectively. The SyN optimization was executed with a cross-correlation radius of 4 voxels, a gradient step size of 0.2, a total deformation field regularization σ = 0.5, and multi-resolution iterations of 2400 × 1200 × 40 across pyramid levels.

Direct synthetic T1w-like-based registration. In this strategy, the synthetic T1w-like volumes were directly registered to the standard NMT template space without intermediate in vivo MRI guidance. The direct composite transformation Φ is formulated as:

$$\Phi = \phi \circ A$$

where A represents global affine alignment and $\phi \in \mathrm{Diff}_0$ denotes direct non-linear SyN diffeomorphic mapping. The resulting transformed optical volume and projected atlas labels are computed via:

$$I_{NMT} = I_{opt} \circ \Phi^{-1}, \quad L_{opt} = L_{NMT} \circ \Phi$$

Global affine alignment was implemented using the identical GC metric configuration as described above. For the non-linear SyN stage, optimization was performed using the CC

metric with a radius of 4 voxels, a gradient step size of 0.2, a total deformation field regularization σ = 0.1, and multi-resolution iterations of 2400 × 1200 × 40 across pyramid levels.

Acknowledgments

The authors used Gemini and ChatGPT for language editing and manuscript polishing. The authors take full responsibility for the final content.

Funding:

This work was partially supported by the National Key R&D Program of China (Grant Nos. 2022YEF0203200 and 2022YFA1603604); the STI2030-Major Projects (2021ZD0200104); the National Natural Science Foundation of China (Grant Nos. 82260227, 61890950, and 62401185); Hainan University Research Start-up Fund (KYQD(ZR)20072 and KYQD(ZR)22074); the PhD Scientific Research and Innovation Foundation of The Education Department of Hainan Province Joint Project of Sanya Yazhou Bay Science and Technology City (HSPHDSRF-2024-08-010).

Competing interests:

The authors declare that they have no competing interests.

Supplementary Materials

The attachment file includes:

Figs. S1 to S15

REFERENCES

1. M. Thiebaut de Schotten, S. J. Forkel, The emergent properties of the connected brain. *Science* **378**, 505–510 (2022).
2. J. Ngai, BRAIN 2.0: Transforming neuroscience. *Cell* **185**, 4–8 (2022).
3. J. Park, J. Wang, W. Guan, L. A. Gjesteby, D. Pollack, L. Kamentsky, N. B. Evans, J. Stirman, X. Gu, C. Zhao, S. Marx, M. E. Kim, S. W. Choi, M. Snyder, D. Chavez, C. Su-Arcaro, Y. Tian, C. S. Park, Q. Zhang, D. H. Yun, M. Moukheiber, G. Feng, X. W. Yang, C. D. Keene, P. R. Hof, S. S. Ghosh, M. P. Frosch, L. J. Brattain, K. Chung, Integrated platform for multiscale molecular imaging and phenotyping of the human brain. *Science* **384**, eadh9979 (2024).
4. J. Langlieb, N. S. Sachdev, K. S. Balderrama, N. M. Nadaf, M. Raj, E. Murray, J. T. Webber, C. Vanderburg, V. Gazestani, D. Tward, C. Mezias, X. Li, K. Flowers, D. M. Cable, T. Norton, P. Mitra, F. Chen, E. Z. Macosko, The molecular cytoarchitecture of the adult mouse brain. *Nature* **624**, 333–342 (2023).

5. K. Amunts, H. Mohlberg, S. Bludau, K. Zilles, Julich-Brain: A 3D probabilistic atlas of the human brain's cytoarchitecture. *Science* **369**, 988–+ (2020).
6. A. Chen, Y. Sun, Y. Lei, C. Li, S. Liao, J. Meng, Y. Bai, Z. Liu, Z. Liang, Z. Zhu, N. Yuan, H. Yang, Z. Wu, F. Lin, K. Wang, M. Li, S. Zhang, M. Yang, T. Fei, Z. Zhuang, Y. Huang, Y. Zhang, Y. Xu, L. Cui, R. Zhang, L. Han, X. Sun, B. Chen, W. Li, B. Huangfu, K. Ma, J. Ma, Z. Li, Y. Lin, H. Wang, Y. Zhong, H. Zhang, Q. Yu, Y. Wang, X. Liu, J. Peng, C. Liu, W. Chen, W. Pan, Y. An, S. Xia, Y. Lu, M. Wang, X. Song, S. Liu, Z. Wang, C. Gong, X. Huang, Y. Yuan, Y. Zhao, Q. Chai, X. Tan, J. Liu, M. Zheng, S. Li, Y. Huang, Y. Hong, Z. Huang, M. Li, M. Jin, Y. Li, H. Zhang, S. Sun, L. Gao, Y. Bai, M. Cheng, G. Hu, S. Liu, B. Wang, B. Xiang, S. Li, H. Li, M. Chen, S. Wang, M. Li, W. Liu, X. Liu, Q. Zhao, M. Lisby, J. Wang, J. Fang, Y. Lin, Q. Xie, Z. Liu, J. He, H. Xu, W. Huang, J. Mulder, H. Yang, Y. Sun, M. Uhlen, M. Poo, J. Wang, J. Yao, W. Wei, Y. Li, Z. Shen, L. Liu, Z. Liu, X. Xu, C. Li, Single-cell spatial transcriptome reveals cell-type organization in the macaque cortex. *Cell* **186**, 3726–3743 e3724 (2023).
7. Z. Yao, C. T. J. van Velthoven, M. Kunst, M. Zhang, D. McMillen, C. Lee, W. Jung, J. Goldy, A. Abdelhak, M. Aitken, K. Baker, P. Baker, E. Barkan, D. Bertagnolli, A. Bhandiwad, C. Bielstein, P. Bishwakarma, J. Campos, D. Carey, T. Casper, A. B. Chakka, R. Chakrabarty, S. Chavan, M. Chen, M. Clark, J. Close, K. Crichton, S. Daniel, P. DiValentin, T. Dolbeare, L. Ellingwood, E. Fiabane, T. Fliss, J. Gee, J. Gerstenberger, A. Glandon, J. Gloe, J. Gould, J. Gray, N. Guilford, J. Guzman, D. Hirschstein, W. Ho, M. Hooper, M. Huang, M. Hupp, K. Jin, M. Kroll, K. Lathia, A. Leon, S. Li, B. Long, Z. Madigan, J. Malloy, J. Malone, Z. Maltzer, N. Martin, R. McCue, R. McGinty, N. Mei, J. Melchor, E. Meyerdierks, T. Mollenkopf, S. Moonsman, T. N. Nguyen, S. Otto, T. Pham, C. Rimorin, A. Ruiz, R. Sanchez, L. Sawyer, N. Shapovalova, N. Shepard, C. Slaughterbeck, J. Sulc, M. Tieu, A. Torkelson, H. Tung, N. Valera Cuevas, S. Vance, K. Wadhwani, K. Ward, B. Levi, C. Farrell, R. Young, B. Staats, M.-Q. M. Wang, C. L. Thompson, S. Mufti, C. M. Pagan, L. Kruse, N. Dee, S. M. Sunkin, L. Esposito, M. J. Hawrylycz, J. Waters, L. Ng, K. Smith, B. Tasic, X. Zhuang, H. Zeng, A high-resolution transcriptomic and spatial atlas of cell types in the whole mouse brain. *Nature* **624**, 317–332 (2023).
8. S. Qiu, Y. Hu, Y. Huang, T. Gao, X. Wang, D. Wang, B. Ren, X. Shi, Y. Chen, X. Wang, D. Wang, L. Han, Y. Liang, D. Liu, Q. Liu, L. Deng, Z. Chen, L. Zhan, T. Chen, Y. Huang, Q. Wu, T. Xie, L. Qian, C. Jin, J. Huang, W. Deng, T. Jiang, X. Li, X. Jia, J. Yuan, A. Li, J. Yan, N. Xu, L. Xu, Q. Luo, M. M. Poo, Y. Sun, C. T. Li, H. Yao, H. Gong, Y. G. Sun, C. Xu, Whole-brain spatial organization of hippocampal single-neuron projectomes. *Science* **383**, eadj9198 (2024).
9. A. Arkhipov, N. da Costa, S. de Vries, T. Bakken, C. Bennett, A. Bernard, J. Berg, M. Buice, F. Collman, T. Daigle, M. Garrett, N. Gouwens, P. A. Groblewski, J. Harris, M. Hawrylycz, R. Hodge, T. Jarsky, B. Kalmbach, J. Lecoq, B. Lee, E. Lein, B. Levi, S. Mihalas, L. Ng, S. Olsen, C. Reid, J. H. Siegle, S. Sorensen, B. Tasic, C. Thompson, J. T. Ting, C. van Velthoven, S. Yao, Z. Yao, C. Koch, H. Zeng, "Integrating multimodal data to understand cortical circuit architecture and function" in *Nat Neurosci* (United States, 2025), vol. 28, pp. 717–730.
10. Q. Wang, S. L. Ding, Y. Li, J. Royall, D. Feng, P. Lesnar, N. Graddis, M. Naeemi, B. Facer, A. Ho, T. Dolbeare, B. Blanchard, N. Dee, W. Wakeman, K. E. Hirokawa, A. Szafer, S. M. Sunkin, S. W. Oh, A. Bernard, J. W. Phillips, M. Hawrylycz, C. Koch, H. Zeng, J. A. Harris, L. Ng, The Allen Mouse Brain Common Coordinate Framework: A 3D Reference Atlas. *Cell* **181**, 936–

953 e920 (2020).

11. Z. Y. Li, Z. Y. Shang, J. Y. Liu, H. T. Zhen, E. T. Zhu, S. L. Zhong, R. N. Sturgess, Y. T. Zhou, X. M. Hu, X. Y. Zhao, Y. Wu, P. Q. Li, R. Lin, J. Ren, D-LMBmap: a fully automated deep-learning pipeline for whole-brain profiling of neural circuitry. *Nature Methods* **20**, 1593–+ (2023).
12. L. Qu, Y. Y. Li, P. Xie, L. J. Liu, Y. M. Wang, J. Wu, Y. Liu, T. Wang, L. F. Li, K. X. Guo, W. Wan, L. Ouyang, F. Xiong, A. C. Kolstad, Z. H. Wu, F. Xu, Y. F. Zheng, H. Gong, Q. M. Luo, G. Q. Bi, H. W. Dong, M. Hawrylycz, H. K. Zeng, H. C. Peng, Cross-modal coherent registration of whole mouse brains. *Nature Methods* **19**, 111–+ (2022).
13. H. Ni, Z. Feng, Y. Guan, X. Y. Jia, W. Chen, T. Jiang, Q. Y. Zhong, J. Yuan, M. Ren, X. N. Li, H. Gong, Q. M. Luo, A. Li, DeepMapi: a Fully Automatic Registration Method for Mesoscopic Optical Brain Images Using Convolutional Neural Networks. *Neuroinformatics* **19**, 267–284 (2021).
14. T. Funck, K. Wagstyl, C. Lepage, M. Omidyeganeh, P. J. Toussaint, T. Xu, K. Amunts, A. Thiel, N. Palomero-Gallagher, A. C. Evans, "Brainbuilder: a software pipeline for 3D reconstruction of cortical maps from multi-modal 2D data sets" in *Commun Biol* (England, 2025), vol. 8, pp. 1015.
15. L. Gou, Y. Wang, L. Gao, S. Liu, M. Wang, Q. Chai, J. Fang, L. Zhan, X. Shen, T. Jiang, W. Ren, M. Ren, X. Jia, C. Xiao, A. Li, X. Li, Q. Luo, G. Okazawa, T. Yang, Z. Liu, M. M. Poo, X. Yang, Z. Shen, C. Xu, J. Yan, Single-neuron projectomes of macaque prefrontal cortex reveal refined axon targeting and arborization. *Cell* **188**, 3806–3822 e3824 (2025).
16. D. C. Van Essen, C. J. Donahue, T. S. Coalson, H. Kennedy, T. Hayashi, M. F. Glasser, Cerebral cortical folding, parcellation, and connectivity in humans, nonhuman primates, and mice. *Proceedings of the National Academy of Sciences* **116**, 26173–26180 (2019).
17. J. Pichat, J. E. Iglesias, T. Yousry, S. Ourselin, M. Modat, A Survey of Methods for 3D Histology Reconstruction. *Med Image Anal* **46**, 73–105 (2018).
18. K. Amunts, C. Lepage, L. Borgeat, H. Mohlberg, T. Dickscheid, M. É. Rousseau, S. Bludau, P. L. Bazin, L. B. Lewis, A. M. Oros-Peusquens, N. J. Shah, T. Lippert, K. Zilles, A. C. Evans, BigBrain: An Ultrahigh-Resolution 3D Human Brain Model. *Science* **340**, 1472–1475 (2013).
19. B. C. Lee, M. K. Lin, Y. Fu, J. Hata, M. I. Miller, P. P. Mitra, Multimodal cross-registration and quantification of metric distortions in marmoset whole brain histology using diffeomorphic mappings. *J Comp Neurol* **529**, 281–295 (2021).
20. J. Seidlitz, C. Sponheim, D. Glen, F. Q. Ye, K. S. Saleem, D. A. Leopold, L. Ungerleider, A. Messinger, A population MRI brain template and analysis tools for the macaque. *Neuroimage* **170**, 121–131 (2018).
21. P. F. Balan, Q. Zhu, X. Li, M. Niu, L. Rapan, T. Funck, H. Wang, R. Bakker, N. Palomero-Gallagher, W. Vanduffel, "MEBRAINS 1.0: A new population-based macaque atlas" in *Imaging Neurosci (Camb)* (United States, 2024), vol. 2.
22. Q. Lv, M. Yan, X. Shen, J. Wu, W. Yu, S. Yan, F. Yang, K. Zeljic, Y. Shi, Z. Zhou, L. Lv, X. Hu, R. Menon, Z. Wang, "Normative Analysis of Individual Brain Differences Based on a Population MRI-Based Atlas of Cynomolgus Macaques" in *Cereb Cortex* (United States, 2021), vol. 31, pp. 341–355.
23. J. Dauguet, T. Delzescaux, F. Conde, J. F. Mangin, N. Ayache, P. Hantraye, V. Frouin,

"Three-dimensional reconstruction of stained histological slices and 3D non-linear registration with in-vivo MRI for whole baboon brain" in *J Neurosci Methods* (Netherlands, 2007), vol. 164, pp. 191–204.

24. M. P. Heinrich, M. Jenkinson, M. Bhushan, T. Matin, F. V. Gleeson, S. M. Brady, J. A. Schnabel, MIND: modality independent neighbourhood descriptor for multi-modal deformable registration. *Med Image Anal* **16**, 1423–1435 (2012).
25. J. E. Iglesias, E. Konukoglu, D. Zikic, B. Glocker, K. Van Leemput, B. Fischl, in *International Conference on Medical Image Computing and Computer-Assisted Intervention*. (Springer, 2013), pp. 631–638.
26. D. Tward, T. Brown, Y. Kageyama, J. Patel, Z. Hou, S. Mori, M. Albert, J. Troncoso, M. Miller, Diffeomorphic Registration With Intensity Transformation and Missing Data: Application to 3D Digital Pathology of Alzheimer's Disease. *Front Neurosci* **14**, 52 (2020).
27. P. A. Yushkevich, M. Munoz Lopez, M. M. Iniguez de Onzono Martin, R. Ittyerah, S. Lim, S. Ravikumar, M. L. Bedard, S. Pickup, W. Liu, J. Wang, L. Y. Hung, J. Lasserve, N. Vergnet, L. Xie, M. Dong, S. Cui, L. McCollum, J. L. Robinson, T. Schuck, R. de Flores, M. Grossman, M. D. Tisdall, K. Prabhakaran, G. Mizsei, S. R. Das, E. Artacho-Perula, M. D. M. Arroyo Jimenez, M. P. Marcos Raba, F. J. Molina Romero, S. Cebada Sanchez, J. C. Delgado Gonzalez, C. de la Rosa-Prieto, M. Corcoles Parada, E. B. Lee, J. Q. Trojanowski, D. T. Ohm, L. E. M. Wisse, D. A. Wolk, D. J. Irwin, R. Insausti, "Three-dimensional mapping of neurofibrillary tangle burden in the human medial temporal lobe" in *Brain* (England, 2021), vol. 144, pp. 2784–2797.
28. D. Ortega-Cruz, K. S. Bress, H. Gazula, A. Rabano, J. E. Iglesias, B. A. Strange, "Three-dimensional histology reveals dissociable human hippocampal long-axis gradients of Alzheimer's pathology" in *Alzheimers Dement* (United States, 2024), vol. 20, pp. 2606–2619.
29. A. Casamitjana, M. Mancini, E. Robinson, L. Peter, R. Annunziata, J. Althonayan, S. Crampsie, E. Blackburn, B. Billot, A. Atzeni, O. Puonti, Y. Balbastre, P. Schmidt, J. Hughes, J. C. Augustinack, B. L. Edlow, L. Zollei, D. L. Thomas, D. Kliemann, M. Bocchetta, C. Strand, J. L. Holton, Z. Jaunmuktane, J. E. Iglesias, "A probabilistic histological atlas of the human brain for MRI segmentation" in *Nature* (England, 2025), vol. 648, pp. 678–685.
30. C. Zhou, X. Yang, S. Wu, Q. Zhong, T. Luo, A. Li, G. Liu, Q. Sun, P. Luo, L. Deng, H. Ni, C. Tan, J. Yuan, Q. Luo, X. Hu, X. Li, H. Gong, Continuous subcellular resolution three-dimensional imaging on intact macaque brain. *Sci Bull (Beijing)* **67**, 85–96 (2022).
31. M. Wang, Y. Hou, L. Magrou, J. A. Autio, P. Misery, T. Coalson, E. Reid, Y. Xu, C. Lamy, A. Falchier, Q. Zhang, M.-M. Poo, C. Dehay, M. F. Glasser, T. Hayashi, K. Knoblauch, D. Van Essen, Z. Shen, H. Kennedy, Retinotopic organization of feedback projections in primate early visual cortex: implications for active vision. *bioRxiv*, 2022.2004.2027.489651 (2022).
32. W.-T. Chen, A. Lu, K. Craessaerts, B. Pavie, C. S. Frigerio, N. Corthout, X. Qian, J. Laláková, M. Kühnemund, I. Voytyuk, Spatial transcriptomics and in situ sequencing to study Alzheimer's disease. *Cell* **182**, 976–991. e919 (2020).
33. H. Carey, M. Pegios, L. Martin, C. Saleeba, A. J. Turner, N. A. Everett, I. E. Bjerke, M. A. Puchades, J. G. Bjaalie, S. McMullan, DeepSlice: rapid fully automatic registration of mouse brain imaging to a volumetric atlas. *Nature Communications* **14**, 5884 (2023).
34. A. Alkemade, P.-L. Bazin, R. Balesar, K. Pine, E. Kirilina, H. E. Möller, R. Trampel, J. M. Kros,

M. C. Keuken, R. L. A. W. Bleys, D. F. Swaab, A. Herrler, N. Weiskopf, B. U. Forstmann, A unified 3D map of microscopic architecture and MRI of the human brain. *Science Advances* **8**, eabj7892 (2022).

35. B. B. Avants, N. Tustison, G. Song, Advanced normalization tools (ANTS). *Insight j* **2**, 1–35 (2009).
36. M. K. Lin, Y. S. Takahashi, B. X. Huo, M. Hanada, J. Nagashima, J. Hata, A. S. Tolpygo, K. Ram, B. C. Lee, M. I. Miller, M. G. Rosa, E. Sasaki, A. Iriki, H. Okano, P. Mitra, "A high-throughput neurohistological pipeline for brain-wide mesoscale connectivity mapping of the common marmoset" in *Elife* (England, 2019), vol. 8.
37. Y. Lei, Y. Liu, M. Wang, N. Yuan, Y. Hou, L. Ding, Z. Zhu, Z. Wu, C. Li, M. Zheng, Single-cell spatial transcriptome atlas and whole-brain connectivity of the macaque claustrum. *Cell* **188**, 3863–3881. e3825 (2025).
38. N. T. Markov, M. M. Ercsey-Ravasz, A. R. Ribeiro Gomes, C. Lamy, L. Magrou, J. Vezoli, P. Misery, A. Falchier, R. Quilodran, M. A. Gariel, J. Sallet, R. Gamanut, C. Huissoud, S. Clavagnier, P. Giroud, D. Sappey-Marinier, P. Barone, C. Dehay, Z. Toroczkai, K. Knoblauch, D. C. Van Essen, H. Kennedy, A Weighted and Directed Interareal Connectivity Matrix for Macaque Cerebral Cortex. *Cerebral Cortex* **24**, 17–36 (2014).
39. J. A. Charbonneau, S. B. Carp, J. L. Bennett, S. M. Maw, G. Moadab, J. P. Christianson, M. G. Baxter, E. Bliss-Moreau, Comparative insights into insula structure and function. *Nature Neuroscience*, (2026).
40. M.-M. Mesulam, E. J. Mufson, Insula of the old world monkey. Architectonics in the insulo-orbito-temporal component of the paralimbic brain. *Journal of Comparative Neurology* **212**, 1–22 (1982).
41. E. J. Mufson, M.-M. Mesulam, Insula of the old world monkey. II: Afferent cortical input and comments on the claustrum. *Journal of Comparative Neurology* **212**, 23–37 (1982).
42. M.-M. Mesulam, E. J. Mufson, Insula of the old world monkey. III: Efferent cortical output and comments on function. *Journal of Comparative Neurology* **212**, 38–52 (1982).
43. R. B. Mars, J. Sallet, F.-X. Neubert, M. F. S. Rushworth, Connectivity profiles reveal the relationship between brain areas for social cognition in human and monkey temporoparietal cortex. *Proceedings of the National Academy of Sciences* **110**, 10806–10811 (2013).
44. Y. Lu, Y. Cui, L. Cao, Z. Dong, L. Cheng, W. Wu, C. Wang, X. Liu, Y. Liu, B. Zhang, D. Li, B. Zhao, H. Wang, K. Li, L. Ma, W. Shi, W. Li, Y. Ma, Z. Du, J. Zhang, H. Xiong, N. Luo, Y. Liu, X. Hou, J. Han, H. Sun, T. Cai, Q. Peng, L. Feng, J. Wang, G. Paxinos, Z. Yang, L. Fan, T. Jiang, Macaque Brainnetome Atlas: A multifaceted brain map with parcellation, connection, and histology. *Sci Bull (Beijing)* **69**, 2241–2259 (2024).
45. F. Xu, Y. Shen, L. Ding, C.-Y. Yang, H. Tan, H. Wang, Q. Zhu, R. Xu, F. Wu, Y. Xiao, C. Xu, Q. Li, P. Su, L. I. Zhang, H.-W. Dong, R. Desimone, F. Xu, X. Hu, P.-M. Lau, G.-Q. Bi, High-throughput mapping of a whole rhesus monkey brain at micrometer resolution. *Nature Biotechnology* **39**, 1521–1528 (2021).
46. Y. Luo, X. Li, C. Zhou, G. Liu, X. Jia, X. Yang, A. Li, H. Gong, Z. Feng, Mapping sagittal-plane reference brain atlas of the cynomolgus macaque (Macaca fascicularis) based on consecutive cytoarchitectonic images. *Brain Structure and Function* **229**, 2045–2057 (2024).

47. R. Hartig, D. Glen, B. Jung, N. K. Logothetis, G. Paxinos, E. A. Garza-Villarreal, A. Messinger, H. C. Evrard, The Subcortical Atlas of the Rhesus Macaque (SARM) for neuroimaging. *Neuroimage* **235**, 117996 (2021).
48. C. Reveley, A. Gruslys, F. Q. Ye, D. Glen, J. Samaha, B. E. Russ, Z. Saad, A. K. Seth, D. A. Leopold, K. S. Saleem, Three-Dimensional Digital Template Atlas of the Macaque Brain. *Cerebral Cortex*, (2016).
49. B. Jung, P. A. Taylor, J. Seidlitz, C. Sponheim, P. Perkins, L. G. Ungerleider, D. Glen, A. Messinger, A comprehensive macaque fMRI pipeline and hierarchical atlas. *NeuroImage* **235**, 117997 (2021).
50. C. Reveley, A. Gruslys, F. Q. Ye, D. Glen, J. Samaha, E. R. B, Z. Saad, K. S. A, D. A. Leopold, K. S. Saleem, Three-Dimensional Digital Template Atlas of the Macaque Brain. *Cereb Cortex* **27**, 4463–4477 (2017).
51. N. Ravi, V. Gabeur, Y.-T. Hu, R. Hu, C. Ryali, T. Ma, H. Khedr, R. Rädle, C. Rolland, L. Gustafson, E. Mintun, J. Pan, K. Vasudev Alwala, N. Carion, C.-Y. Wu, R. Girshick, P. Dollár, C. Feichtenhofer, SAM 2: Segment Anything in Images and Videos. 10.48550/arXiv.2408.00714 (2024).
52. J.-Y. a. P. Zhu, Taesung and Isola, Phillip and Efros, Alexei A., in *Proceedings of the IEEE International Conference on Computer Vision (ICCV)*. (2017), pp. 2242–2251.
53. A. Gu, T. Dao, Mamba: Linear-Time Sequence Modeling with Selective State Spaces. 10.48550/arXiv.2312.00752 (2023).
54. K. He, X. Zhang, S. Ren, J. Sun, in *2016 IEEE Conference on Computer Vision and Pattern Recognition Workshops (CVPRW)*. (IEEE, Las Vegas, NV, 2016), pp. 1.
55. P. Isola, J.-Y. Zhu, T. Zhou, A. A. Efros, Image-to-Image Translation with Conditional Adversarial Networks. 10.48550/arXiv.1611.07004 (2016).
56. R. A. Shahaf E. Finder, Eran Treister, Oren Freifeld, Wavelet Convolutions for Large Receptive Fields. (2024).
57. X. Mao, Q. Li, H. Xie, R. Y. K. Lau, Z. Wang, S. P. Smolley, in *2017 IEEE International Conference on Computer Vision (ICCV)*. (2017), pp. 2813–2821.

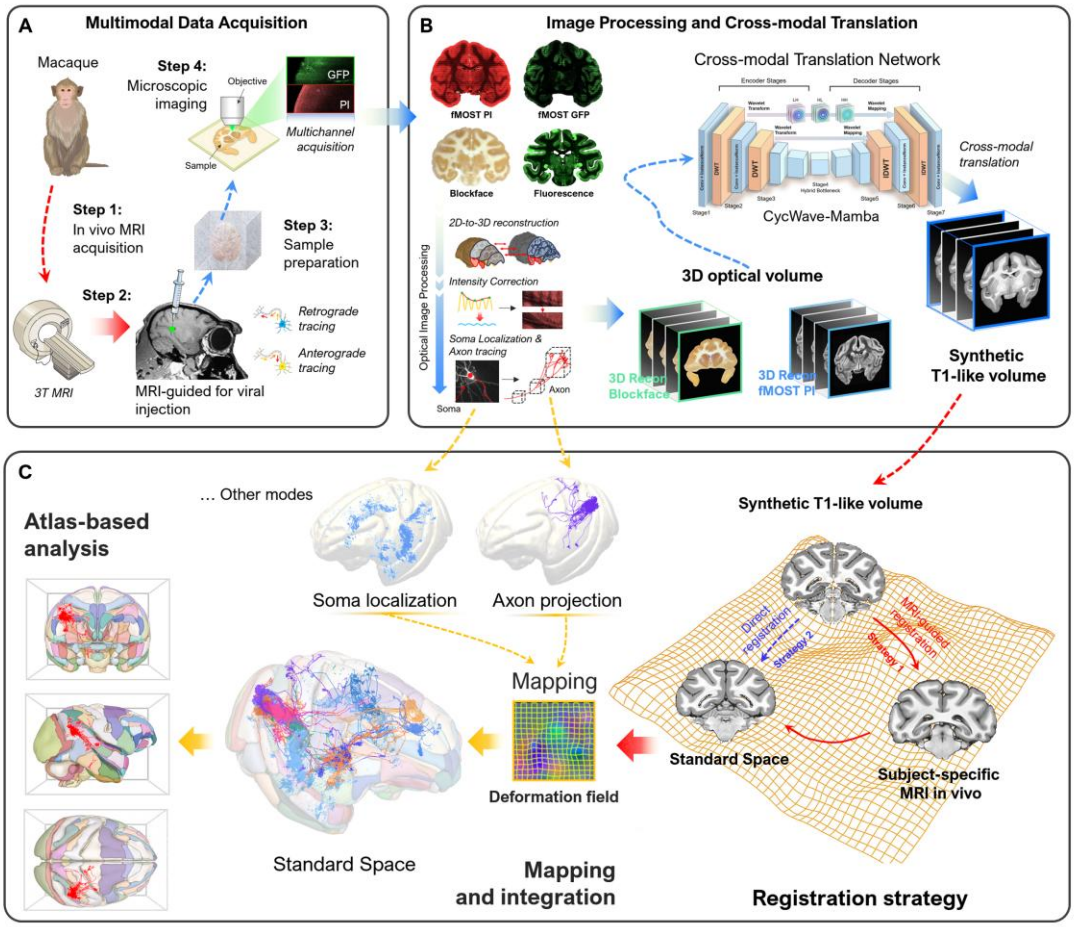


Fig. 1. Overview of Macaca-Star. (**A**) Experimental workflow in which subject-specific in vivo MRI was first acquired to localize injection targets, followed by viral injection, sample preparation, and ex vivo optical imaging (**B**) Image processing and cross-modal translation. Acquired optical images undergo modality-specific preprocessing to generate reconstructed block-face and fMOST PI volumes. These structural volumes are then translated by CycWave-Mamba into synthetic T1w MRI-like volumes. fMOST GFP datasets are used for axon tracing, whereas 2D fluorescence sections are processed for soma localization. (**C**) Synthetic T1-like images generated from fMOST PI or block-face volumes were registered to the NMT template directly or with subject-specific in vivo MRI guidance. The resulting transformations were applied to map axonal projections, soma locations, and other derived data into NMT space for atlas-based quantification and statistical analysis.

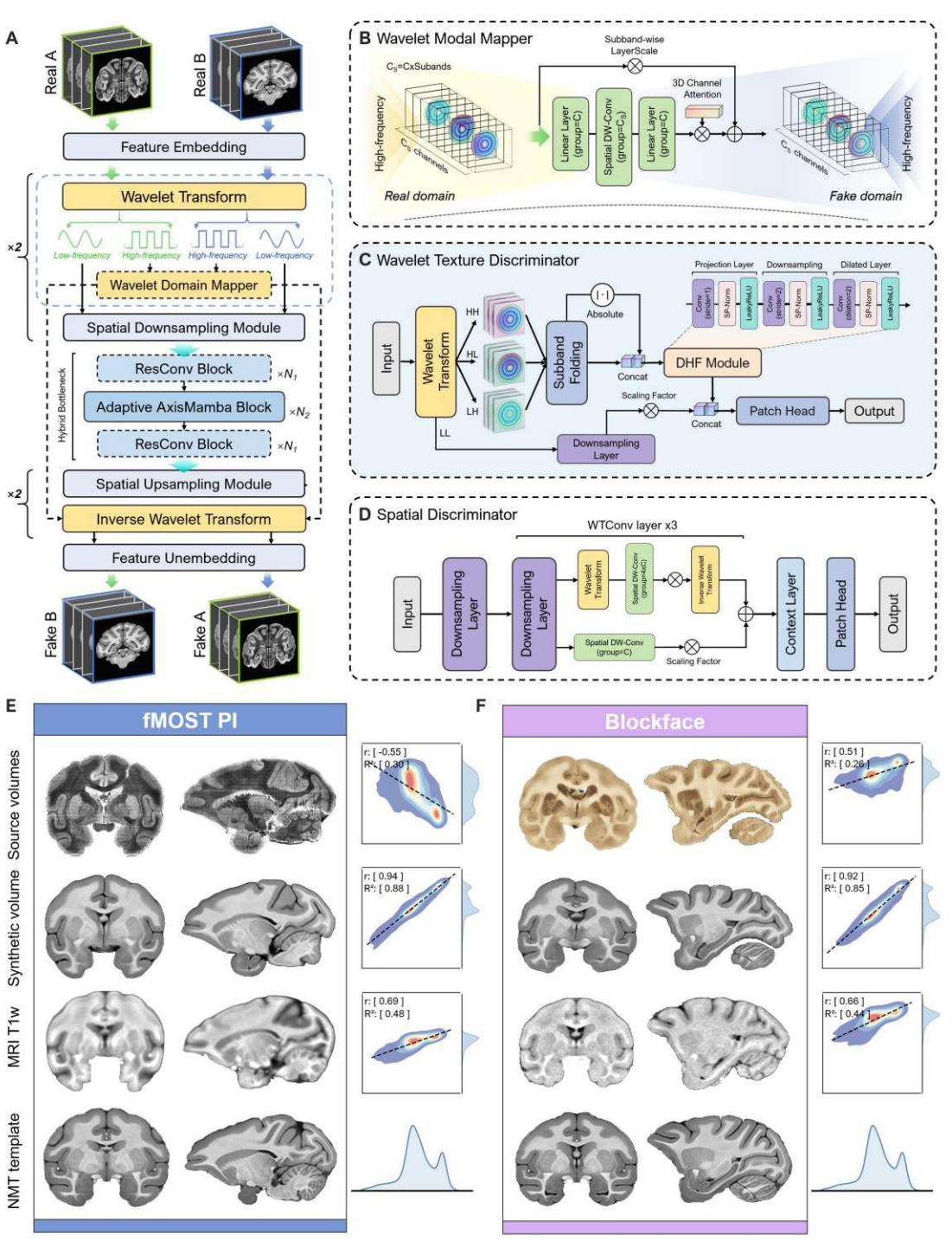


Fig. 2. CycWave-Mamba architecture and cross-modal evaluation. (**A**) 3D generator architecture. Synthesizes T1w MRI targets from 3D optical volumes (fMOST PI or block-face) by combining DWT feature decomposition, a hybrid ResNet-Mamba bottleneck for global semantics, and IDWT reconstruction to preserve anatomical fidelity. (**B**) Wavelet Modal Mapper. This module processes high-frequency subbands across total channels C_S = C×subbands (where C denotes the channels per subband), incorporating cross-subband feature refinement, gated channel attention, and learnable residual fusion for cross-modal texture translation. (**C**) Wavelet Texture Discriminator. Operating in the frequency domain via DWT, this network processes high-frequency subbands concatenated with their absolute

magnitudes, employing spectral-normalized dilated convolutions for patch-level adversarial texture discrimination. (**D**) Spatial Discriminator. This 3D PatchGAN incorporates wavelet convolutions (WTConv3d_D) with parallel spatial and frequency pathways to expand effective receptive fields, enforcing global spatial and anatomical consistency. (**E, F**) Synthesis Results and Evaluation. Rows 1–4 show the source volume, synthetic volume, MRI T1w, and NMT template for fMOST PI (E) and Blockface (F). Right columns show topographic intensity correlation maps with annotated r and R^2.

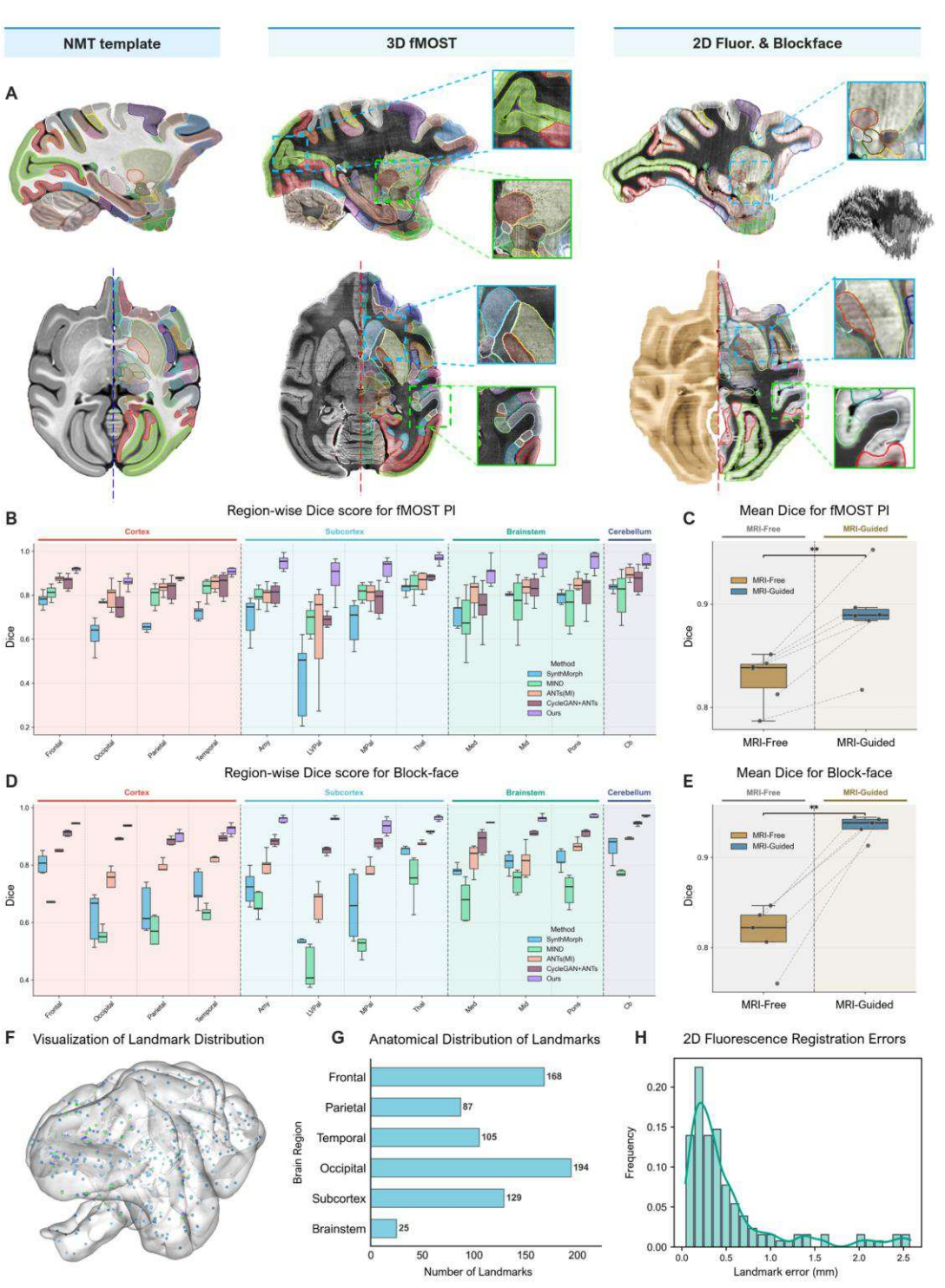


Fig. 3. Evaluation of cross-modal registration accuracy. (**A**) Representative registration results. Left to right: target NMT template (sagittal, top; horizontal, bottom), registered fMOST PI, and fused view of block-face (left hemisphere) and 3D-reconstructed fluorescence (right hemisphere). Color-coded NMT cortical and subcortical atlas labels are directly mapped onto the sagittal and horizontal slices of each modality. (**B, D**) Quantitative evaluation and method comparisons of registration accuracy on 9 fMOST PI (B) and 5 block-face (D) macaque brains. Region-wise Dice scores across four cortical lobes, subcortical nuclei, and major subregions

of the brainstem and cerebellum are presented for different registration methods. (**C, E**) Comparison of MRI-Guided and MRI-Free registration strategies. Evaluations were performed on 9 fMOST PI (C) and 5 3D block-face (E) macaque brains. For each subject, subject-level mean Dice scores were calculated by averaging across finer anatomical subdivisions at level 4 for both CHARM and SARM atlases. (**F**) Paired landmarks are displayed within the 3D macaque brain topology to evaluate 2D registration accuracy. Points were annotated at corresponding anatomical structures between block-face sections and registered fluorescence slices. (**G**) Anatomical distribution of landmarks. Regional counts of the paired landmarks from f across four cortical lobes, subcortical regions, and the brainstem. (**H**) 2D fluorescence registration errors. Magnitude distribution of 2D landmark registration errors across fluorescence sections, presented as a histogram.

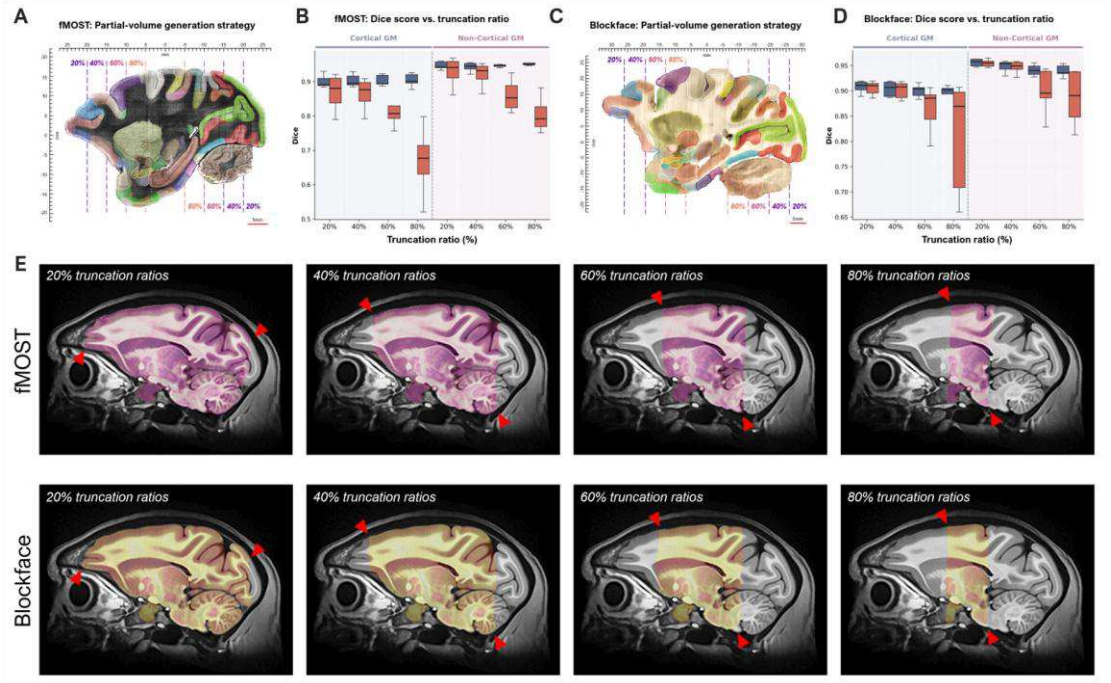


Fig. 4. Evaluation of partial-volume registration (**A, C**) Partial-volume generation strategy and spatial scale in fMOST (A) and block-face imaging (C). Representative sagittal sections illustrate partial brain volumes generated by progressively truncating tissue along the anterior–posterior axis, with lines indicating spatial boundaries. (**B, D**) Quantitative registration accuracy across different truncation ratios in fMOST (B) and block-face imaging (D), evaluated using Dice scores under MRI-guided versus MRI-free conditions. (**E**) Qualitative registration results across varying truncation ratios. Registered partial volumes of fMOST (top) and block-face imaging (bottom) are transparently overlaid onto the canonical NMT reference template.

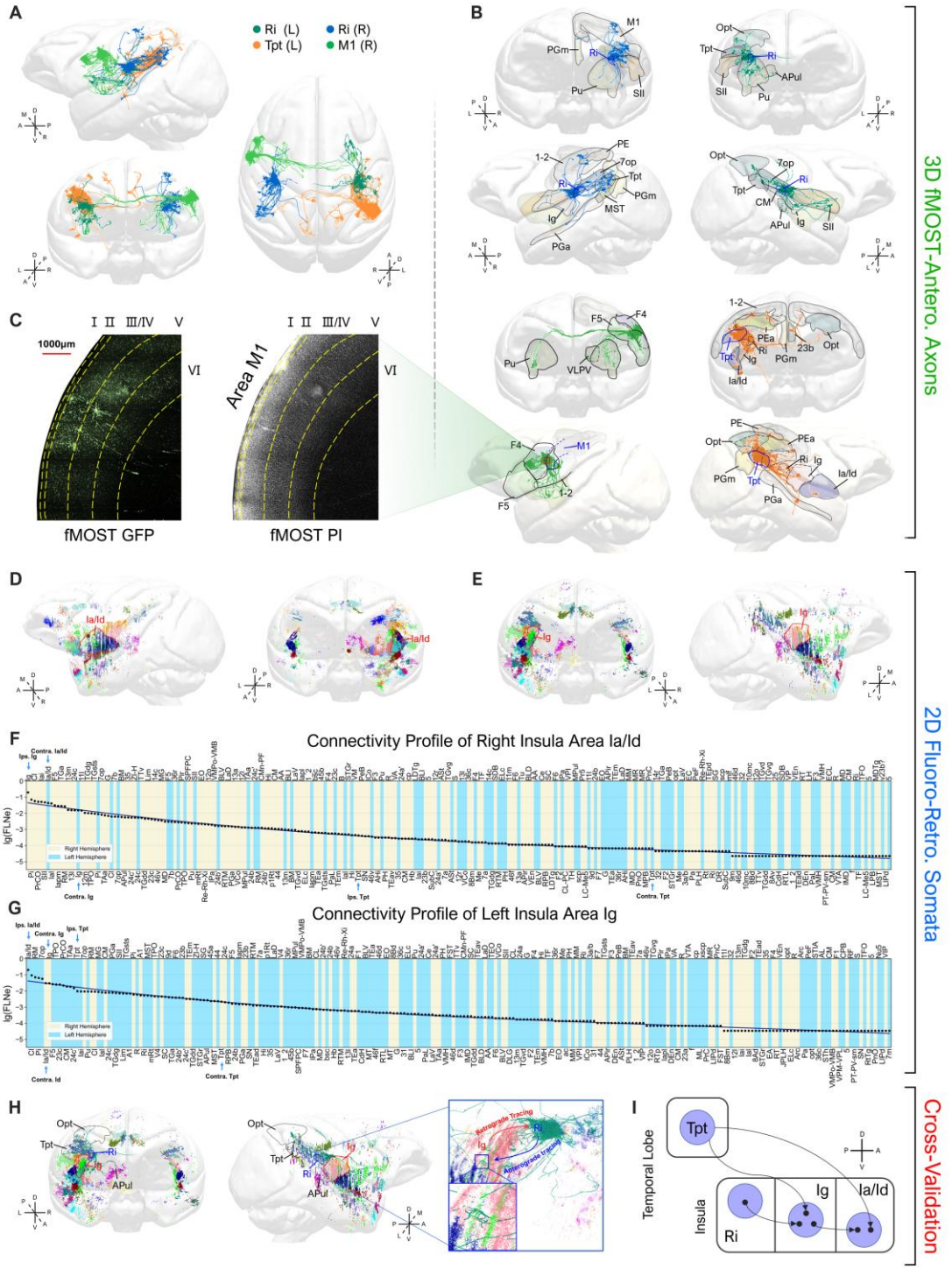


Fig. 5. Atlas-based integration of axonal projections and somata. (**A**) 3D stereotaxic integration of GFP-labeled neuronal projection pathways originating from four distinct injection sites within standard space, color-coded by injection site and presented from three orthogonal views (anterior, superior, and lateral). (**B**) Individual 3D visualizations of projection patterns for each injection site, with annotated injection locations and target brain regions. (**C**) Cortical laminar organization at the primary motor cortex (M1) injection site, partitioned into five distinct layers, with layers III and IV merged into a single layer. (**D**, **E**) Spatial mapping of soma distributions from 2D fluorescence sections into standard space, where somata are

color-coded according to their corresponding atlas subregions. (**F**, **G**) Regional distribution of the fraction of labeled neurons (FLNe) across cortical areas for Id (F) and Ig (G) injections, calculated from the mapped somata in (D, E). (**H**) Spatial integration of anterograde fMOST axonal projections and retrograde soma distributions in standard space. Axonal projections originating from the retroinsular area (Ri) extend into the granular insula (Ig), overlapping with retrogradely labeled somata in Ri originating from an Ig injection. (**I**) Schematic circuit model summarizing the multi-region projection hierarchy, where each connection was cross-validated via paired anterograde fMOST and retrograde soma tracing (as demonstrated in H). Tpt directly projects to Ri, Ig, and Id; additionally, inter-areal projections exist among these regions, extending from Ri to Ig, and from Ig to Id.

Supplementary Files

This is a list of supplementary files associated with this preprint. Click to download.

- SupplementaryMaterials.docx